Detecting strong gravitational lensing of gravitational waves with TianQin

Xin-yi Lin (林心怡)[,1] Jian-dong Zhang (张建东)[,1,*] Liang Dai (戴亮)[,2,†]
Shun-Jia Huang (黄顺佳)[,1] and Jianwei Mei (梅健伟)[1]

[1]*MOE Key Labortory of TianQin Mission, TianQin Research Center for Gravitational Physics
and School of Physics and Astronomy, Frontiers Science Center for TianQin,
CNSA Research Center for Gravitational Waves, Sun Yat-sen University (Zhuhai Campus),
Zhuhai 519082, China*
[2]*Department of Physics, University of California,
366 Physics North MC 7300, Berkeley, California 94720, USA*

When gravitational waves (GWs) pass by a massive object on its way to Earth, a strong gravitational lensing effect will happen. Thus, the GW signal will be amplified, deflected, and delayed in time. Through analyzing the lensed GW waveform, physical properties of the lens can be inferred. On the other hand, neglecting lensing effects in the analysis of GW data may induce systematic errors in the estimating of source parameters. As a space-borne GW detector, TianQin will be launched in the 2030s. It is expected to detect dozens of mergers of massive black hole binaries (MBHBs) as far as $z = 15$ and thus will have high probability to detect at least one lensed event during the mission lifetime. In this article, we discuss the capability of TianQin to detect lensed MBHB signals. Three lens models are considered in this work: the point mass model, the singular isothermal sphere (SIS) model, and the Navarro-Frenk-White (NFW) model. The sensitive frequency band for space-borne GW detectors is around millihertz, and the corresponding GW wavelength could be comparable to the lens gravitational length scale, which requires us to account for wave diffraction effects. In calculating lensed waveforms, we adopt the approximation of geometric optics at high frequencies to accelerate computation, while precisely evaluating the diffraction integral at low frequencies. Through a Fisher analysis, we analyze the accuracy to estimate the lens parameters. We find that the accuracy can reach to the level of 10^{-3} for the mass of point mass and SIS lens and to the level of 10^{-5} for the density of the NFW lens. We also assess the impact on the accuracy of estimating the source parameters and find that the improvement of the accuracy is dominated by the increasing of signal-to-noise ratio.

I. INTRODUCTION

When electromagnetic waves pass near a massive object, they are deflected, delayed, and amplified. This is known as the gravitational lensing effect [1]. Gravitational lensing has a wide range of applications in the study of cosmology, the large scale structure, exoplanets, dark matter, and so on. Similar to electromagnetic waves, gravitational waves (GWs) may also be lensed [2]. We can use lensed GW signals to study the nature of dark matter, the property of GWs, and probe cosmology [3–16].

Gravitational waves from merging binary compact objects have been detected by the LIGO/Virgo/KAGRA Collaboration (LVK) [17]. Thus far, 90 events have been confirmed by the LVK and announced in the Gravitational-Wave Transient Catalog [18–21]. Many studies have been conducted on gravitational lensing of gravitational wave signals [3,22–36], although no convincing candidates of lensed GW sources have been reported. Nevertheless, prospects are high that many lensed GW events will be found by next-generation GW detectors such as the Einstein Telescope and Cosmic Explorer [37,38].

In the near future, space-borne GW observatories such as LISA [39] and TianQin [40] are expected to discover hundreds of mergers of massive black hole binaries (MBHBs) [41,42]. In a previous study [43], it was argued that almost 1% of the detected events may experience strong gravitational lensing. Although the estimation may be inaccurate due to simplification of the model, it is highly likely that lensed GW signals at low frequencies will be detected at future space-borne GW detectors. There is a method that can be used to study the lensing of GWs emitted by massive black hole binary mergers at high redshift [44].

If the wavelength is much shorter than the gravitational radius of the lens, geometrical optics is applicable to the calculation of the lensing effect. In the regime of strong lensing, we may observe multiple signals that originate

[*]zhangjd9@mail.sysu.edu.cn
[†]liangdai@berkeley.edu

from the same source and arrive at different times with different observed wave strengths.

However, if the GW wavelength is comparable to or longer than the gravitational length of the lens, wave optics must be used in the calculation, which requires accurate evaluation of the diffraction integral. For example, if GWs in the LVK band are lensed by stars, intermediate-massive black holes (IMBHs), or other objects, they behave much like light diffraction in the wave optics regime [45–48]. The wave optics effect can perturb the plane of GW polarization [49,50] and cause beat patterns in the time-domain waveform [51,52]. These effects might allow LVK to detect massive stars, IMBHs, the dense cores of globular clusters, and dark matter halos [53–60]. The space-borne GW detectors will focus on the millihertz band; thus they may observe a variety of sources such as Galactic ultra-compact binaries [61–63], coalescing massive black holes [42,64,65], low frequency inspirals of stellar-mass black holes [66–69], extreme-mass-ratio inspirals [70–72], and the stochastic GW backgrounds [47,73,74]. Because of high event rates and the capacity in testing the nature of gravity and black holes (BHs), MBHBs are one of the most important sources. It can also be used to probe the nature of BHs and gravity [75–78]. In this work, we will focus on the lensing of GW signals from MBHBs events.

GWs emitted by MBHBs detectable by LISA allow the possibility for wave optics effects of lensing to be detected [79,80]. However, the sensitive band for TianQin will be a little bit higher than LISA, so we need to consider the wave optics and geometric optics separately for different parts of the signals. In the calculation of the diffraction integral, many different methods have been developed in previous works [81–84]. In calculating the geometrical optics effects, beyond the leading order effect, we will consider the subleading order effect (i.e., the postgeometric correction) following the method in [85]. This improves the accuracy in evaluating the diffraction integral and enables a smooth connection between results approximated in the wave diffraction regime and in the geometrical optics regime.

In this paper, we analyzed the ability of TianQin on the parameter estimation for the source and the lens object. We also consider LISA as a comparison. We consider three parametrized models for the lens, namely, the point mass model, the singular isothermal sphere (SIS) model, and the Navarro-Frenk-White (NFW) model. We compare unlensed and lensed cases and quantify the precision improvement in source parameter inference. We choose the coalescence of MBHBs of equal masses $10^6 M_\odot$ as a fiducial GW source. The accuracy in the source parameter inference sees an increase due to increased SNR caused by magnification in lensing. As for the lens parameters, we focus on parameter measurement accuracy of space-based GW observatories. The best fractional uncertainty in measuring the lens parameters is about 10^{-3} for point mass and the SIS model and 10^{-5} for the NFW model.

The remainder of the paper will be organized as follows. In Sec. II, we introduce the model for unlensed GW signals as well as the detector response functions to be used in this work. In Sec. III, we discuss the effect of gravitational lensing on GWs, both in the regime of geometrical optics and in the regime of wave optics. In Sec. IV, we study the amplification factor $F(f)$ with different lens models and examine the results in both regimes. In Sec. VI, we present the ability to estimate the parameters of the sources and lenses for TianQin and LISA. In Sec. VII, we summarize results and discuss related issues. Throughout this work, the geometrized unit system ($G = c = 1$) is used.

II. WAVEFORM MODEL

As one of the most important GW sources for space-borne GW detectors such as TianQin, MBHBs is expected to have the chance to be gravitationally lensed. In this work, we use the phenomenological waveform model IMRPhenomD [86] to characterize its waveform including inspiral, merger, and ringdown. The list of source parameters we take into account in parameter inference are η, M, t_c, D_L, θ_S, ϕ_S, ι, and ψ. Here $M = m_1 + m_2$ is the total mass of the binary, $\eta = m_1 m_2 / M^2$ is the symmetric mass ratio, t_c is the coalescence time, and D_L is the luminosity distance at the source redshift z_S. θ_S and ϕ_S are two angles that parametrize the source position on the sky in the detector coordinate system. ι and ψ are the inclination angle and polarization angle, respectively. In each Michelson channel of the interferometer, the strain $h(t)$ can be decomposed into the superposition of two linear polarizations [41]

$$h_\alpha(t) = \frac{\sqrt{3}}{2}\left[F_\alpha^+(t)h_+(t - t_D) + F_\alpha^\times(t)h_\times(t - t_D)\right], \quad (1)$$

where $\alpha = 1, 2$ denotes the two Michelson channels of the TianQin constellation, and t_D is the difference in the light travel time between the interferometer and the solar system barycenter,

$$t_D = R \sin\bar{\theta}_S \cos[\bar{\Phi}(t) - \bar{\phi}_S]. \quad (2)$$

According to the planned orbital configuration of the TianQin satellite constellation, we choose $R = 1$ AU and $\bar{\Phi}(t) = \bar{\phi}_0 + 2\pi t/T$, where $T = 1$ yr, and $\bar{\phi}_0$ is the initial orbital phase of TianQin at time $t = 0$. The angles $(\bar{\theta}_S, \bar{\phi}_S)$ are the orientation of the detector in the heliocentric ecliptic coordinates.

The waveform is provided in the frequency domain, while the antenna pattern functions F_α^+ and $F_\alpha^\times$ are conveniently expressed as functions of time. Therefore, we take the detected frequency-domain strain signal $\tilde{h}_\alpha(f)$ computed as the Fourier transform of the time-domain signal as given by Eq. (1) [66],

$$\tilde{h}_\alpha(f) = \frac{\sqrt{3}}{2} \left\{ \mathcal{F}[h_+(t - t_D)F_\alpha^+(t)] + \mathcal{F}[h_\times(t - t_D)F_\alpha^\times(t)] \right\}, \tag{3}$$

where $\mathcal{F}[\ldots]$ denotes Fourier transformation. The results of Fourier transformation, for the two Michelson channels $\alpha = 1, 2$, are given in [66] as

$$\mathcal{F}[h_+(t - t_D)F_1^+(t)] = \frac{1}{4}(1 + \cos^2\theta_S)\cos 2\psi_S \left[e^{2i\zeta_1(f - 2f_0)}\tilde{h}_+(f - 2f_0) + e^{-2i\zeta_2(f + 2f_0)}\tilde{h}_+(f + 2f_0) \right]$$

$$- \frac{i}{2}\cos\theta_S \sin 2\psi_S \left[-e^{2i\zeta_1(f - 2f_0)}\tilde{h}_+(f - 2f_0) + e^{-2i\zeta_2(f + 2f_0)}\tilde{h}_+(f + 2f_0) \right],$$

$$\mathcal{F}[h_\times(t - t_D)F_1^\times(t)] = \frac{1}{4}(1 + \cos^2\theta_S)\sin 2\psi_S \left[e^{2i\zeta_1(f - 2f_0)}\tilde{h}_\times(f - 2f_0) + e^{-2i\zeta_2(f + 2f_0)}\tilde{h}_\times(f + 2f_0) \right]$$

$$+ \frac{i}{2}\cos\theta_S \cos 2\psi_S \left[-e^{2i\zeta_1(f - 2f_0)}\tilde{h}_\times(f - 2f_0) + e^{-2i\zeta_2(f + 2f_0)}\tilde{h}_\times(f + 2f_0) \right],$$

$$\mathcal{F}[h_+(t - t_D)F_2^+(t)] = \mathcal{F}\left[h_+(t - t_D)F_1^+\left(\phi_{S0} - \frac{\pi}{4}\right) \right],$$

$$\mathcal{F}[h_\times(t - t_D)F_2^\times(t)] = \mathcal{F}\left[h_\times(t - t_D)F_1^\times\left(\phi_{S0} - \frac{\pi}{4}\right) \right], \tag{4}$$

where we introduce two functions of the frequency, $\zeta_1(f) = \phi_{S0} - \pi f t_D$ and $\zeta_2(f) = \phi_{S0} + \pi f t_D$, and ψ_S is the polarization angle. f_0 is the frequency at which TianQin satellites orbit Earth, and ϕ_{S0} is the initial position of the source in detector's coordinate frame. As for the detector response for LISA, we take Eq. (27) in [2].

III. LENSING EFFECT

At a fixed frequency f, the gravitationally lensed waveforms $\tilde{h}_{+,\times}^L(f)$ are related to the unlensed waveforms through

$$\tilde{h}_{+,\times}^L(f) = F(f)\tilde{h}_{+,\times}(f), \tag{5}$$

where the multiplicative, complex-valued amplification factor $F(f)$ [87] is given by the diffraction integral [57,88,89]

$$F(f) = \frac{f(1 + z_L)}{i} \frac{d_L d_S}{c d_{LS}} \int d^2\mathbf{x} e^{i2\pi f(1 + z_L)\tau(\mathbf{x})}, \tag{6}$$

where $\mathbf{x}$ are the angular coordinates that parametrize the two-dimensional lens plane, d_L, d_S, and d_{LS} are the angular diameter distances to lens at redshift z_L, that to the source at redshift z_S, and that between the lens and the source, respectively. The ray travel time $\tau(\mathbf{x})$ is given by the sum of the geometrical delay and the gravitational Shapiro delay,

$$\tau(\mathbf{x}) = \frac{d_L d_S}{c d_{LS}}\left(\frac{1}{2}|\mathbf{x} - \mathbf{y}|^2 - \phi(\mathbf{x}) + \phi_m(\mathbf{y}) \right), \tag{7}$$

where $\mathbf{y}$ is the dimensionless source position. $\phi(\mathbf{x})$ is the lensing potential. $\phi_m(\mathbf{y})$ is the phase modulation that makes the minimum value of the time delay zero. Note that we set the angular position of the lens at the coordinate origin. The angular position of the source relative to that of the lens, on the other hand, will be accounted for by appropriately shifting the center of the lensing potential function $\phi(\mathbf{x})$.

We rewrite the amplification factor $F(f)$ in terms of the dimensionless quantity

$$w = 2\pi f(1 + z_L)\frac{d_S}{c d_L d_{LS}}\xi^2, \tag{8}$$

where ξ is the normalization constant of the length in the lens plane.

The diffraction integral needs to be performed over the entire lensing plane. This integral is conditionally convergent because the integrand is a highly oscillatory phase factor of unity absolute value. Direct integration of the diffraction integral is well known to be difficult and will typically take a prohibitive amount of time to achieve the desired precision. In order to calculate $F(f)$ more efficiently, we use the asymptotic expansion method. For any smoothly varying function $f(z)$ multiplied by a fast oscillating phase factor, the following integral can be reexpressed as

$$\int_0^\infty dz e^{iwz}f(z) = \int_0^b dz e^{iwz}f(z)$$

$$+ e^{iwb}\sum_{n=1}^\infty \frac{(-1)^n}{(iw)^n}\frac{\partial^{n-1}f}{\partial z^{n-1}}\bigg|_{z=b}. \tag{9}$$

Reference [83] suggests that truncating the infinite series at $n = 7$ achieves sufficient accuracy.

In the low frequency regime, defined by $w \leq 10$, wave diffraction causes amplitude and phase distortions in the complex number $F(f)$. In this wave diffraction regime, we compute $F(f)$ by evaluating the diffraction integral using the asymptotic expansion method explained in the previous paragraph. In the intermediate and high frequency regime, defined by $w > 10$, the result is well approximated by geometric optics, which predicts that the overall amplification factor is the sum of the amplification factor of all geometric images $j = 1, 2, \ldots$. It has the following expression [88–91]:

$$F_{\text{geo}}(w) = \sum_j |\mu_j|^{1/2} e^{i(w\tau_j - \frac{\pi}{2}n_j)}, \tag{10}$$

where the magnification factor of the jth geometric image is given by

$$\mu_j = \left[\det \left(\mathbf{I} - \frac{\partial^2 \phi(\mathbf{x}_j)}{\partial \mathbf{x} \partial \mathbf{x}} \right) \right]^{-1}, \tag{11}$$

where $\mathbf{I}$ is the 2×2 identity matrix, and $\partial^2 \phi / \partial \mathbf{x} \partial \mathbf{x}$ denotes the 2×2 Hessian matrix of the lensing potential $\phi(\mathbf{x})$. We define $\tau_j = \tau(\mathbf{x}_j)$ to be the total light travel time along the ray trajectory corresponding to the jth image and set $n_j = 0, 1, 2$ depending on if the position of the jth image $\mathbf{x}_j$ is a minimum, saddle, or maximum point of $\tau(\mathbf{x})$, respectively [90–92].

In fact, F_{geo} is not an extremely accurate approximation of the exact amplification factor in the intermediate to high frequency regime. Consequently, corrections need to be introduced to improve accuracy. In order to better match the amplification factor in geometrical optics approximation with the exact value, we include the postgeometrical optics correction δF [84,85], which is the sum of terms for correction to the geometric magnification of images δF_m and an additional contribution δF_c from the diffracted image that arises at the cuspy lens center. Including the postgeometric optics correction beyond the geometrical optics limit F can be rewritten as

$$F(w) = \sum_j |\mu_j|^{1/2} \left(1 + \frac{i}{w}\Delta_j \right) e^{i(w\tau_j - \frac{\pi}{2}n_j)}, \tag{12}$$

where

$$\Delta_j = \frac{1}{16} \left[\frac{1}{2\alpha_j^2} \psi_j^{(4)} + \frac{5}{12\alpha_j^3} \psi_j^{(3)2} + \frac{1}{\alpha_j^2} \frac{\psi_j^{(3)}}{|x_j|} + \frac{\alpha_j - \beta_j}{\alpha_j \beta_j} \frac{1}{|x_j|^2} \right], \tag{13}$$

with the coefficients defined as

$$\alpha_j = \frac{1}{2} \left(1 - \frac{d^2\psi(|\mathbf{x}_j|)}{dx^2} \right), \qquad \beta_j = \frac{1}{2} \left(1 - \frac{1}{|x_j|} \frac{d\psi(|\mathbf{x}_j|)}{dx} \right). \tag{14}$$

The second term in Eq. (12) is the correction to the magnification factor of the geometric image,

$$\delta F_m(w) = \frac{i}{w} \sum_j \Delta_j |\mu_j|^{1/2} e^{i(w\tau_j - \frac{\pi}{2}n_j)}. \tag{15}$$

The correction term δF_c arises from the central density cusp of the lens. Different lens models have different δF_c.

IV. LENSING MODEL

To study a range of physical lenses with different mass profiles, we consider three lens models. They are the point mass lens, the singular isothermal sphere, and the Navarro-Frenk-White lens. The point mass lens is the simplest lensing model. The SIS model lens represents the early type galaxies, while the NFW lens is suitable for the lensing models of cold dark matter halos.

A. Point mass lens

The point mass lens has all of its mass concentrated at one point. Its mass density is described by [84,93]

$$\rho(\mathbf{r}) = M_L \delta^3(\mathbf{r}), \tag{16}$$

where M_L is the lens mass. Then ξ can be chosen as the Einstein radius $\xi = r_E = \sqrt{4M_L d_{LS} d_L / d_S}$. The dimensionless lensing potential is $\phi(\mathbf{x}) = \ln |\mathbf{x}|$.

The multiplicative factor $F(f)$ of the point mass lens is [2]

$$F(w) = \exp \left[\frac{\pi w}{4} + \frac{iw}{2} \left(\ln \frac{w}{2} - 2\phi_m(y) \right) \right]$$

$$\times \Gamma \left(1 - \frac{iw}{2} \right) {}_1F_1 \left(\frac{iw}{2}, 1, y^2 \frac{iw}{2} \right), \tag{17}$$

where $\phi_m(y) = (x_m - y)^2/2 - \ln x_m$ with $x_m = (y + \sqrt{y^2 + 4})/2$. Here $\Gamma(z)$ is the Euler gamma function, and ${}_1F_1(a, b, z)$ is Kummer's confluent hypergeometric function.

In the geometric optics regime $w > 10$, the amplification factor is

$$F_{\text{geo}}(w) = |\mu_+|^{1/2} - i|\mu_-|^{1/2} e^{iw\Delta\tau}, \tag{18}$$

where the magnification of the two geometric images are $\mu_\pm = 1/2 \pm (y^2 + 2)/(2y\sqrt{y^2 + 4})$, and the time delay between the two images is

$\Delta\tau = y\sqrt{y^2+4}/2 + \ln[(\sqrt{y^2+4}+y)/(\sqrt{y^2+4}-y)]$.
In the point mass model, the term that corresponds to the diffracted image at the center of lens δF_c is zero [85], and the postgeometric correction to the amplification of the geometric images δF_m is the only contribution to δF. We have

$$\delta F(w) = \frac{i}{3w}\frac{4x_+^2-1}{(x_+^2+1)^3(x_+^2-1)}|\mu_+|^{1/2}$$
$$+ \frac{1}{3w}\frac{4x_-^2-1}{(x_-^2+1)^3(x_-^2-1)}|\mu_-|^{1/2}e^{iw\Delta T}, \quad (19)$$

where $x_\pm = (y \pm \sqrt{y^2+2})/2$ are the positions of both geometric images.

B. Singular isothermal sphere

The SIS lens has a density profile [84,93,94]

$$\rho(\mathbf{r}) = \frac{\sigma_v^2}{2\pi r^2}, \quad (20)$$

where σ_v is the velocity dispersion and ξ can be chosen as the Einstein radius $\xi = r_E = 4\pi\sigma_v^2 d_{LS}d_L/d_S$. Thus, the mass inside this region is $M_{Lz} = 4\pi^2\sigma_v^4(1+z_L)d_L d_{LS}/d_S$. The dimensionless lensing potential is $\phi(\mathbf{x}) = |\mathbf{x}|$.

No close-form analytic result is known for the amplification factor from a SIS lens. In the wave diffraction regime $w < 10$, we rely on calculating the diffraction integral numerically using the asymptotic expansion method introduced before.

In the geometric optics limit, the amplification factor is given by

$$F_{\text{geo}}(w) = \begin{cases} |\mu_+|^{1/2} - i|\mu_-|^{1/2}e^{iw\Delta\tau}, & y < 1, \\ |\mu_+|^{1/2}, & y > 1, \end{cases} \quad (21)$$

where $\mu_\pm = \pm 1 + 1/y$ and $\Delta\tau = 2y$. If $y < 1$, two geometric images form on the image plane. If $y \geq 1$, only a single image forms on the image plane. The postgeometrical optics correction δF is given by

$$\delta F(w) = \frac{i}{w}\frac{1}{(1-y^2)^{3/2}}e^{iw[y^2/2+\phi_m(y)]}$$
$$+ \begin{cases} \frac{i}{8w}\frac{|\mu_+|^{1/2}}{y(y+1)^2} - \frac{1}{8w}\frac{|\mu|^{1/2}}{y(1-y)^2}e^{iw\Delta\tau}, & y < 1, \\ \frac{i}{8w}\frac{|\mu_+|^{1/2}}{y(y+1)^2}, & y > 1, \end{cases} \quad (22)$$

where $\phi_m(y) = y + 1/2$. The first term on the right-hand side of the equation corresponds to the diffracted image forming at the lens' cuspy center, while the remaining terms are postgeometric corrections to the amplification of the geometric image(s).

C. Navarro-Frenk-White lens

The NFW model was first proposed by Navarro, Frenk, and White to describe the density profile of gravitationally bound cold dark matter halos seen in numerical N-body simulations of structure formation [95]. The density profile of the NFW lens can be expressed as [94]

$$\rho(r) = \frac{\rho_s}{(r/r_s)(r/r_s+1)^2}, \quad (23)$$

where r_s is the scale length and ρ_s is the characteristic density. The corresponding lensing potential is analytically derived to be [96,97]

$$\phi(x) = \frac{\kappa_s}{2}\begin{cases} (\ln\frac{x}{2})^2 - \left(\text{arctanh}\sqrt{1-x^2}\right)^2, & x < 1, \\ (\ln\frac{x}{2})^2 + \left(\arctan\sqrt{x^2-1}\right)^2, & x > 1, \end{cases} \quad (24)$$

where $\kappa_s = 16\pi\rho_s(d_L d_{LS}/d_S)r_s$ is the characteristic dimensionless surface mass density (or the characteristic lensing convergence) of the lens.

Since the Einstein radius of NFW lens does not have an analytic form, we choose the scale radius r_s as the normalization length ξ instead of the Einstein radius. In the same way we treat the SIS lens, in the low frequency regime the amplification factor $F(f)$ is numerically calculated using the asymptotic expansion method. When $y < y_{\text{cr}}$, there are three images. Whereas, when $y > y_{\text{cr}}$, only one image is formed.

Unlike what is done for the point mass lens and the SIS lens, the position of the radial caustic y_{cr}, the positions of the geometric images x_j, and their corresponding magnification factors μ_j and time delays T_j are all computed by numerically solving the ray equation of geometric optics. As a result, the amplification factor in the geometric optics limit F_{geo} is obtained numerically. The postgeometric optics correction to the amplification factor is given by

$$\delta F(w) = \frac{i}{w}\sum_j \Delta_j|\mu_j|^{1/2}e^{i(w\tau_j-\pi n_j)} + \frac{\kappa_s}{(wy^2)^2}e^{iw(y^2/2+\phi_m(y))}, \quad (25)$$

where the first term comes from the corrections for the magnifications of the images, and the second term is the diffracted image at the lens center.

V. SIGNAL-TO-NOISE RATIO AND FISHER INFORMATION MATRIX

In GW data analysis, the inner product between two strain time series $a(t)$ and $b(t)$ is defined as

$$(a|b) = 4\Re\mathfrak{e}\int_0^\infty df\frac{\tilde{a}(f)\tilde{b}^*(f)}{S_N(f)}, \quad (26)$$

where $\tilde{a}(f)$ and $\tilde{b}(f)$ are the Fourier transform of time series $a(t)$ and $b(t)$, respectively, the asterisk denotes complex conjugation, and $S_N(f)$ is the one-sided power spectral density (PSD) for the strain noise in the detector under consideration.

The expected noise PSD of TianQin can be approximated by the following analytic expression [40]:

$$S_N(f) = \frac{1}{L^2}\left[\frac{S_a}{(2\pi f)^4}\left(1 + \frac{10^{-4}\,\text{Hz}}{f}\right) + S_x\right], \quad (27)$$

with the acceleration noise $S_a = 1 \times 10^{-30}\,\text{m}^2\,\text{s}^{-4}\,\text{Hz}^{-1}$, the displacement measurement noise $S_x = 1 \times 10^{-24}\,\text{m}^2\,\text{Hz}^{-1}$, and the arm length $L = \sqrt{3} \times 10^5$ km. The estimated noise PSD of LISA can be found in [98].

For a GW signal $h(t)$ and a given detector, the SNR ρ is defined as the square root of the inner product of itself,

$$\rho = (h|h)^{1/2} = \left[4\mathfrak{Re}\int_0^\infty df\,\frac{|\tilde{h}(f)|^2}{S_n(f)}\right]^{1/2}. \quad (28)$$

We follow the Fisher information matrix formalism [99] to estimate the precision of parameter inference. In the limit of large signal-to-noise ratios, the parameter estimation uncertainty for parameters θ^i and $\Delta\theta^i$ have a multivariate Gaussian distribution,

$$p(\Delta\vec{\theta}) = N e^{-\frac{1}{2}\Gamma_{ij}\Delta\theta^i\Delta\theta^j}. \quad (29)$$

Here, the inverse covariance matrix Γ_{ij} is identified with the Fisher information matrix, which can be calculated as

$$\Gamma_{ij} = \left(\frac{\partial h}{\partial\theta^i}\middle|\frac{\partial h}{\partial\theta^j}\right). \quad (30)$$

The appropriate normalization factor is given by $N = \sqrt{\det(\Gamma/2\pi)}$. The root-mean-square of θ^i is given by

$$\sqrt{\langle(\Delta\theta^i)^2\rangle} = \sqrt{\Sigma^{ii}}, \quad (31)$$

where $\Sigma = \Gamma^{-1}$ is the inverse of the Fisher matrix.

VI. PARAMETER ESTIMATION FOR THE LENS OBJECTS

In this section, we exhibit the precision of parameter estimation (PE) for source parameters and lens parameters with lensed GW signals. As a default choice of the parameters, we choose the redshift of the MBHB equal to $z_s = 1$ and the time of coalescence $t_c = 0$. We also set the angle parameters as $\theta_S = \pi/3$, $\phi_S = \pi/3$, $\iota = \pi/6$, and $\psi = \pi/6$. The lens object is set as $z_L = 0.5$. We assume the operation time of TianQin and LISA to be five years. Because the detector plane of TianQin is nearly

perpendicular to the ecliptic plane, the sunlight may enter the telescopes directly if the sun is nearly coplanar with the detector plane. In order to protect the optical system from sunlight, TianQin will adopt the "3 months on + 3 months off" observation scheme, and thus the effective observation time is 2.5 years.

A. Source parameters

As for source parameters, we take η and M_z as examples, and other parameters have similar behavior. In Fig. 1, we exhibit the SNR and the precisions increased due to the lensing effect for η and M_z in the point mass model, with $y = 0.3$. The horizontal axes are chosen to be the redshifted mass of source M_z and lens M_{Lz}. In addition to the increase of SNR relative to the unlensed case plotted in solid lines, we also plot the improvement of the precision for η and M in dotted and dashed lines, respectively. The red and blue lines are the result for TianQin (TQ) and LISA. The upper panel of Fig. 1 shows the SNR and the precisions increase
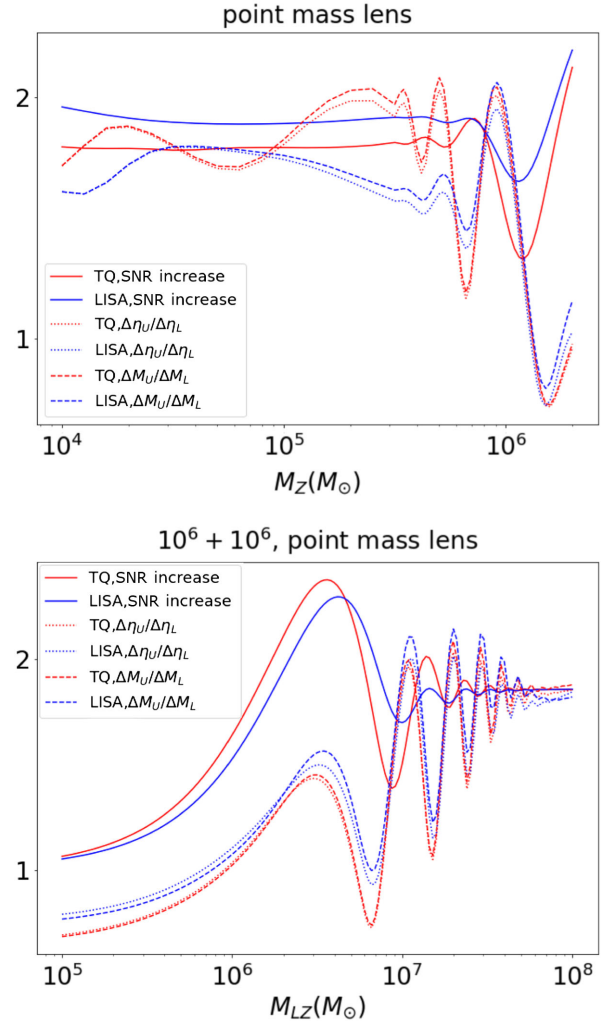
FIG. 1. The SNR and precisions increase of η and M_z with the variation of M_{Lz} and M_z with point mass lens.

of η and M_z with the variation of M_z, and the redshifted lens mass is chosen to be $M_{Lz} = 10^7 M_\odot$. The lower panel of Fig. 1 shows the SNR and the precisions increase of η and M_z with the variation of M_{Lz}, and the redshifted total mass is chosen to be $M_z = 2 \times 10^6 M_\odot$.

We can learn from Fig. 1 that the improvements on the PE accuracy of source parameters are mainly due to the increase of SNR. If the mass of the source is small enough, or the mass of the lens is large enough, the geometric optic effect will dominate the result, thus we can see that the improvement on the PE accuracy is almost proportional to the increase of SNR. However, in the wave effect dominated region it will have some fluctuations, but it is still dominated by the effect of SNR.

The result for the SIS model with $y = 0.3$ is plotted in Fig. 2, corresponding to the case of (upper) $M_{Lz} = 10^7 M_\odot$ with varying M_z and (lower) $M_z = 2 \times 10^6 M_\odot$ with varying M_{Lz}. The result for the NFW model is plotted in Fig. 3. We only consider the case of varying M_z with
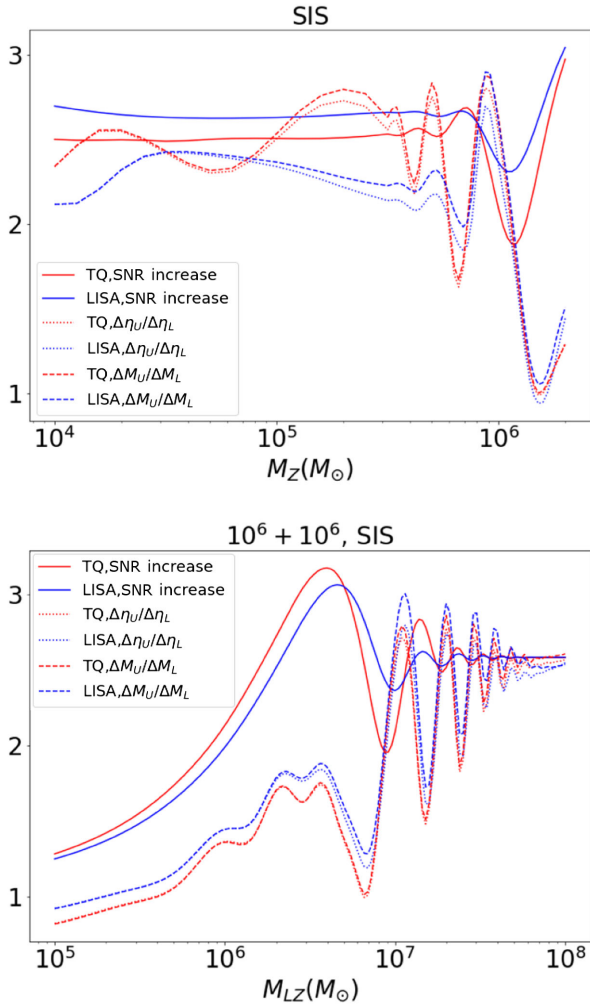
FIG. 2. The SNR and precisions increase of η and M_z with the variation of M_{Lz} and M_z with SIS lens.
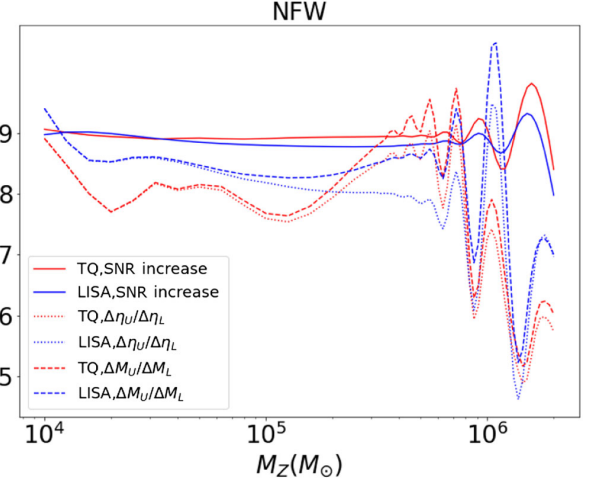
FIG. 3. The SNR and precisions increase of η and M_z with the variation of M_z with NFW lens.

$\kappa_s = 1, r_s = 0.4$ kpc and $y = 0.3$. We can find that, for all three lens models, the increase of the PE accuracy of the source parameters is dominated by the increase of the SNR due to the lensing effect. For the geometric optic region, they will have a linear relationship, but there will exist some fluctuations in the wave optic region.

B. Lens parameters

In this part, we choose the total mass of the MBHB as $10^6 + 10^6 M_\odot$, and thus the SNRs of the unlensed signal are 4285 and 7541 for TianQin and LISA, respectively.

1. Point mass lens

In Fig. 4, we show the precesions of M_{Lz} (upper) and y (lower) with the variaion of M_{Lz} for different values of y. The solid and dashed lines are the estimation errors of M_{Lz} of TianQin and LISA, respectively. In the upper panel, we plot the estimation errors of M_{Lz} with the variation of M_{Lz} with $y = 0.1$, $y = 0.3$, $y = 1$, and $y = 3$ in different colors. The curves in the lower panel are the estimation errors of y with the variation of M_{Lz} with these different y. In general, the trend of the estimation errors declines. When M_{Lz} is large enough, the precisions of lens parameters become stable. It is obvious that the estimation ability of $y = 1$ is best, and the estimation ability of $y = 0.3$ is better than that of $y = 0.1$. However, if y is too large, such as $y = 3$, the estimation ability will be worse. Comparing the curve of $y = 0.1$ and $y = 3$, we can find that the estimation errors of $y = 3$ converge more rapidly, but the estimation ability is worse when the estimation errors converge. The larger y is, the more quickly estimation errors converge. The best accuracy of lens parameters with the point mass model is about 10^{-3}. The estimation ability of LISA is better than TianQin, and this is mainly caused by the higher SNR of LISA, which is about 1.8 times the SNR of TianQin for the

FIG. 4. The precisions of M_{Lz} and y of different y with the variation of M_{Lz}.
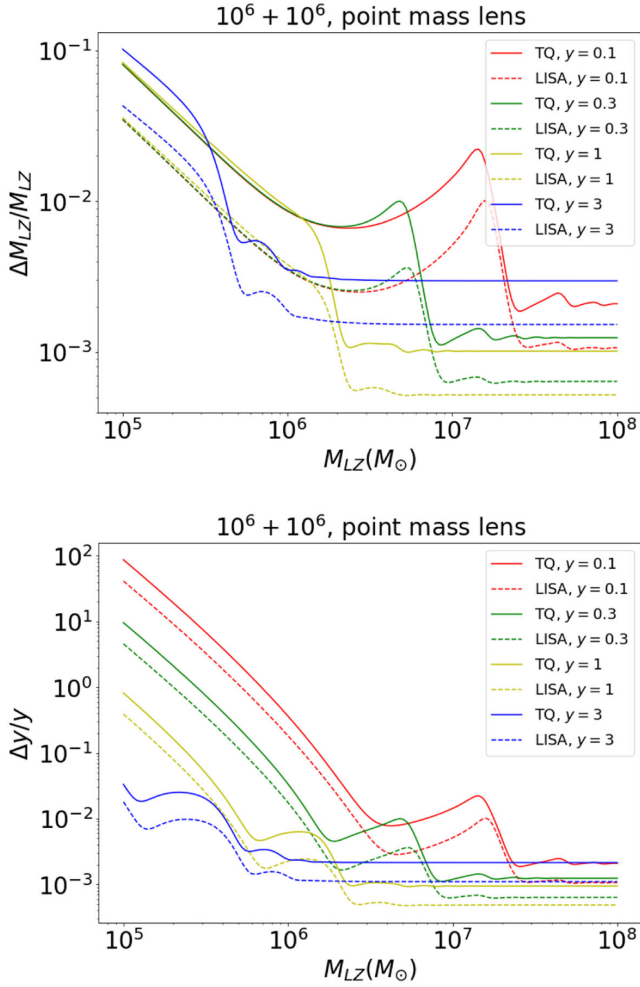
FIG. 5. The precisions of M_{Lz} and y of different M_{Lz} with the variation of y.

source with $10^6 + 10^6 M_\odot$. This feature can also be found for SIS and NFW models in Figs. 6–8.

We also exhibit the precisions of M_{Lz} and y of different M_{Lz} with the variation of y in Fig. 5. In the upper panel, the curves in different colors are the estimation errors of M_{Lz} with the variation of y with $M_{Lz} = 10^6 M_\odot$, $M_{Lz} = 10^7 M_\odot$, and $M_{Lz} = 10^8 M_\odot$, respectively. The estimation errors of y with the variation of y for different M_{Lz} are plotted in the lower panel. When $M_{Lz} = 10^8 M_\odot$, the blue curves in the upper panel are almost the same as those in the lower panel. The parameter estimation accuracy of M_{Lz} is better for $10^{-2} < y < 10$. Similarly, the green curves in the upper panel are almost the same as those in the lower panel, too. When $y < 10^{-1}$, the estimation errors of M_{Lz} are stable. When $10^{-1} < y < 10$, the accuracy of M_{Lz} is best. In the case that $M_{Lz} = 10^6 M_\odot$, if y is smaller than 1, the estimation errors of M_{Lz} will be stable. In other words, if y is small enough, the curves will be stable. While y approaches 1, the accuracy of M_{Lz} will approach its best value. When y equals 10, the value of the negative
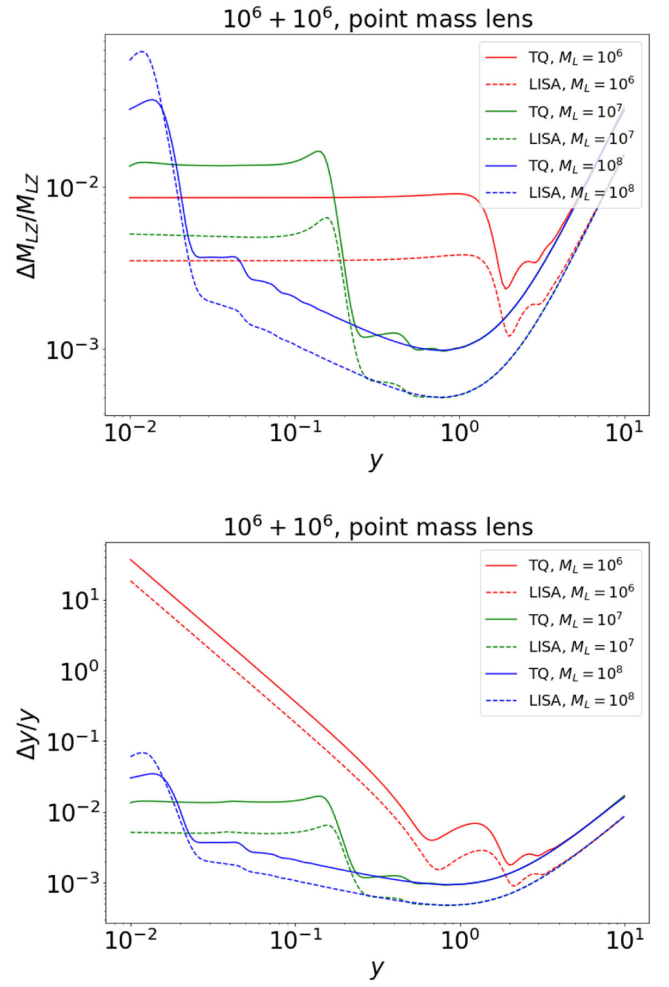
magnification μ_- is about 10^{-4}, and thus the second image is almost invisible. We can take this situation as the case of that without lensing.

2. Singular isothermal sphere

The estimation errors calculated from SIS are exhibited in Figs. 6 and 7 for TianQin in solid lines and for LISA in dashes lines. In the upper panel of Fig. 6, we plot the estimation errors of M_{Lz} with the variation of M_{Lz} with $y = 0.1$, $y = 0.3$, and $y = 3$ in different colors. In the lower panel of Fig. 6, the lines in different colors are the estimation errors of y with the variation of M_{Lz} for different y. We can learn from Eq. (22) that if $y = 1$, there will be a singularity, so we do not consider this situation in Fig. 6. When $y = 0.1$ or $y = 0.3$, if $M_{Lz} > 10^7 M_\odot$, the estimation errors of lens parameters tend to be stable. Instead, when $y = 3$ and $M_{Lz} > 10^6 M_\odot$, if M_{Lz} becomes larger, the estimation errors of lens parameters will become larger too. If M_{Lz} is close to $10^6 M_\odot$, the accuracy of lens parameters will be best. The best accuracy of lens
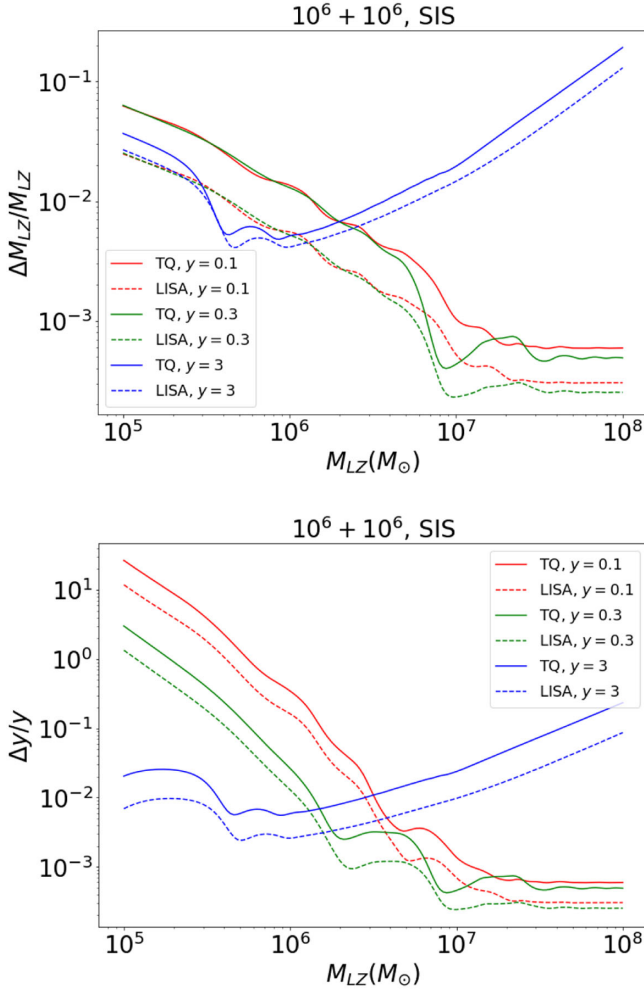
FIG. 6. The precisions of M_{Lz} and y of different y with the variation of M_{Lz}.

FIG. 7. The precisions of M_{Lz} and y of different M_{Lz} with the variation of y.

parameters with the SIS model is about 10^{-3} and a little better than that with the point mass model. The estimation ability of LISA is slightly better than TianQin.

Then, we show the estimation errors of M_{Lz} and y of different M_{Lz} with the variation of y in Fig. 7, and the results for TianQin and LISA are plotted in solid and dashed lines, respectively. The curves with different colors on the upper panel correspond to the estimation errors of M_{Lz} with the variation of y with different M_{Lz}. In the lower panel, these different curves are the estimation errors of y with the variation of y with different M_{Lz}. When $y < 1$, the estimation errors of M_{Lz} are stable. When y approaches 1, we calculate the amplification factor $F(f)$ and $\partial F(f)/\partial \theta_i$ using the diffraction integral. We can learn from Fig. 7 that the estimation errors of M_{Lz} are oscillating in the geometrical optics approximation. In the lower panel of Fig. 7, when $M_{Lz} = 10^6 M_\odot$, if y is small enough, such as smaller than 10^{-2}, the curves of estimation errors of y will become stable. However, when $M_{Lz} = 10^8 M_\odot$, in this case the estimation errors are stable. When y is near 1, the estimation abilities are best.
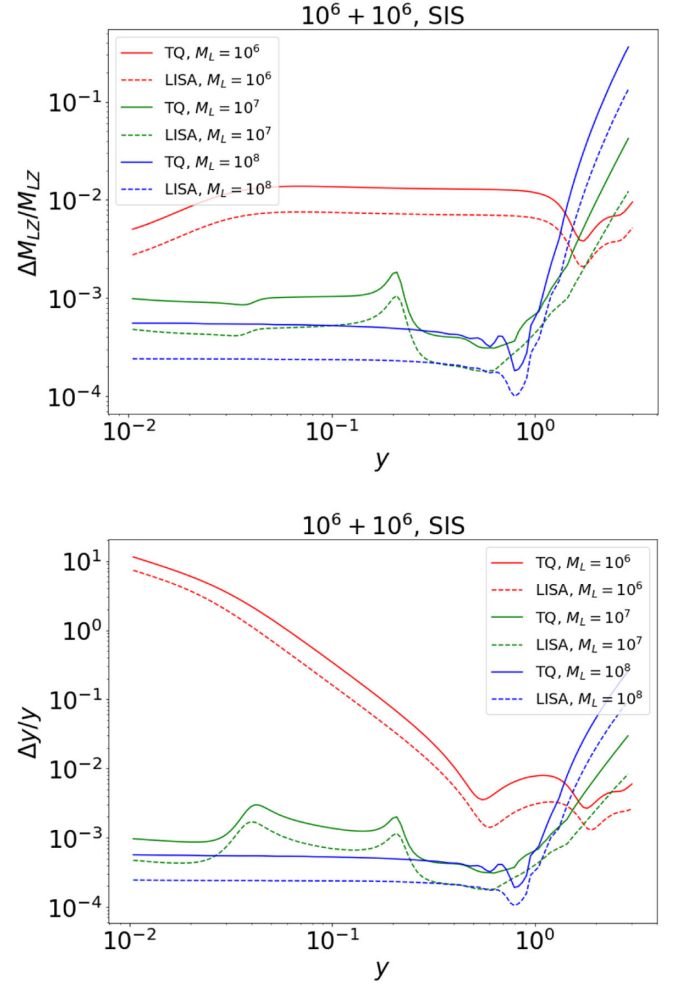
3. Navarro-Frenk-White lens

For the NFW model, we plot the estimation errors of κ_s and y of different κ_s with the variation of y in Fig. 8. Since the main purpose of this work is to consider wave diffraction effects, we choose $r_s = 0.4$ kpc for $\kappa_s = 1$ and $r_s = 0.01$ kpc for $\kappa_s = 10$. Thus, the corresponding M_{200} will be about $4 \times 10^9 M_\odot$ and $5 \times 10^7 M_\odot$, respectively. While these examples correspond to very different values of r_s and M_{200}, they exhibit wave diffraction distortion to the amplitude and phase of the waveform at similar levels. The results for TianQin and LISA are plotted in solid and dashed lines, respectively. In the upper panel of Fig. 8, the curves are the estimation errors of κ_s for different y, with red curves for $\kappa_s = 1$ and green curves for $\kappa_s = 10$. In the lower panel of Fig. 8, the curves are the estimation errors of y with the variation of y. The upper and lower panels of Fig. 8 are similar. When y is less than 1 y_{cr}, the curves are almost smooth. If y is close to the radial caustic, there will be a peak in every curve. As expected, if y is more than 1 y_{cr}, the larger y is, the larger the estimation errors
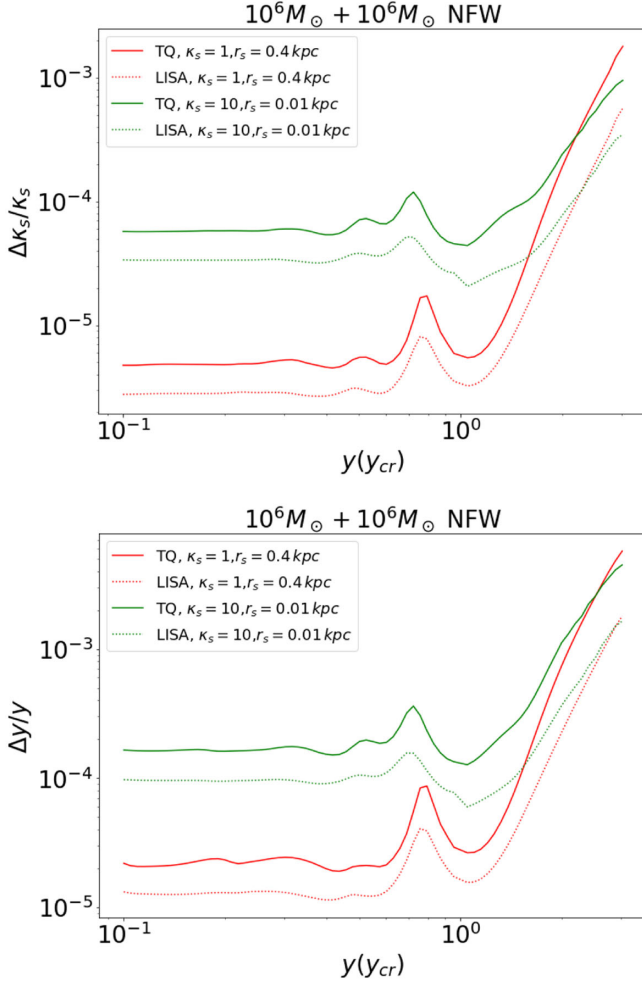
FIG. 8. The precisions of κ_s and y of different κ_s with the variation of y.

are. The same as in the SIS model, the upper limit of y is 3 because we cannot calculate the case where $y > 3$ correctly. However, like the point mass model and SIS model, if y keeps going larger, the errors will also be larger. What is more, when $\kappa_s = 1$, the y_{cr} is small. So the impact parameter is small. If $y < 2y_{cr}$, the estimation errors are especially small. When $\kappa_s = 10$, the estimation errors are still smaller than the other two models because the absolute value of y is small enough. The smallest error is about 10^{-6} when $\kappa_s = 1$, and the smallest error is about 10^{-5} when $\kappa_s = 10$.

VII. CONCLUSION AND DISCUSSION

In this work, we analyze the detection of the gravitational lensing effect of gravitational waves. In the calculation, we consider three types of lensing models: the point mass lens, the SIS lens, and the NFW lens. For each lens model, we calculate the amplification factor in diffraction limit for the

lower frequency part and in geometric optics limit for the higher frequency part. For the geometric optics calculation, we consider both the leading order geometric optics part and the first order postgeometric optics part, and thus the amplification factor for the connection frequency band will be continuous.

For the parameter estimation analysis, we use the Fisher information matrix method. We consider the effect both on the source parameters, and the PE accuracy on the lens parameters. For the source parameters, we find that, due to the increase of SNR caused by lensing effect, the PE accuracy will also be higher than the case without lensing. Moreover, the improvement on the accuracy is almost proportional to the improvement on the SNR, while the influence of the source mass and the lens mass is not significant.

Another important approach is to measure the parameters of the lens with the lensed gravitational signal. We consider both the impact parameter y and the parameter that characterized the total mass of the lens, which is M_{Lz} for the point mass and SIS models and κ_s for the NFW model. We find that the parameter of the source, such as the total mass or the mass ratio, will not affect the PE accuracy of the lens parameters significantly, so we choose the equal mass binary source that constitutes two $10^6 M_\odot$ black holes. For the point mass and SIS models, the mass of the lens can be measured to the level of 10^{-3} for the best cases, and the PE accuracy will approach a constant as the is lens heavy enough. For the NFW model, the characteristic density can be measured to the level of 10^{-5}. For all the cases, the result will diverge as y become larger and larger, since the lensing effect can be neglected at that time. The PE accuracy of LISA is higher then TianQin, since for the signal we consider, LISA has a better sensitivity.

Our current work has assumed that the signal is lensed, and the lens is described by some special lensing model. However, this could not be achieved easily. So, in the future, we expect to study how to identify the lensing event in the GW data and whether we can distinguish different types of lensing models with the lensed signal.

[1] P. Schneider, C. S. Kochanek, and J. Wambsganss, *Gravitational Lensing: Strong, Weak and Micro* (Springer, Berlin, 2006), https://ui.adsabs.harvard.edu/abs/2006glsw.conf.....M/abstract.

[2] R. Takahashi and T. Nakamura, Astrophys. J. **595,** 1039 (2003).

[3] X.-L. Fan, K. Liao, M. Biesiada, A. Piorkowska-Kurpas, and Z.-H. Zhu, Phys. Rev. Lett. **118,** 091102 (2017).

[4] K. Liao, X. Ding, M. Biesiada, X.-L. Fan, and Z.-H. Zhu, Astrophys. J. **867,** 69 (2018).

[5] T. Yang, B. Hu, R.-G. Cai, and B. Wang, Astrophys. J. **880,** 50 (2019).

[6] O. A. Hannuksela, T. E. Collett, M. Çalışkan, and T. G. F. Li, Mon. Not. R. Astron. Soc. **498,** 3395 (2020).

[7] M. Sereno, P. Jetzer, A. Sesana, and M. Volonteri, Mon. Not. R. Astron. Soc. **415,** 2773 (2011).

[8] K. Liao, X.-L. Fan, X.-H. Ding, M. Biesiada, and Z.-H. Zhu, Nat. Commun. **8,** 1148 (2017); **8,** 2136(E) (2017).

[9] S. Cao, J. Qi, Z. Cao, M. Biesiada, J. Li, Y. Pan, and Z.-H. Zhu, Sci. Rep. **9,** 11608 (2019).

[10] Y. Li, X. Fan, and L. Gou, Astrophys. J. **873,** 37 (2019).

[11] H. Yu, P. Zhang, and F.-Y. Wang, Mon. Not. R. Astron. Soc. **497,** 204 (2020).

[12] H. Zhou, Z. Li, K. Liao, and Z. Huang, Mon. Not. R. Astron. Soc. **518,** 149 (2022).

[13] J. Urrutia and V. Vaskonen, Mon. Not. R. Astron. Soc. **509,** 1358 (2021).

[14] A. K.-W. Chung and T. G. F. Li, Phys. Rev. D **104,** 124060 (2021).

[15] J. Gais, K. K. Y. Ng, E. Seo, K. W. K. Wong, and T. G. F. Li, Astrophys. J. Lett. **932,** L4 (2022).

[16] T. Broadhurst, J. M. Diego, and G. F. Smoot, arXiv:2006.13219.

[17] B. P. Abbott *et al.* (LIGO Scientific and Virgo Collaborations), Phys. Rev. Lett. **116,** 061102 (2016).

[18] B. P. Abbott *et al.* (LIGO Scientific and Virgo Collaborations), Phys. Rev. X **9,** 031040 (2019).

[19] R. Abbott *et al.* (LIGO Scientific and Virgo Collaborations), Phys. Rev. X **11,** 021053 (2021).

[20] R. Abbott *et al.* (LIGO Scientific and Virgo Collaborations), arXiv:2108.01045.

[21] R. Abbott *et al.* (LIGO Scientific, Virgo, and KAGRA Collaborations), Astrophys. J. **949,** 76 (2023).

[22] T. Broadhurst, J. M. Diego, and G. F. Smoot, arXiv:1901.03190.

[23] L. P. Singer, D. A. Goldstein, and J. S. Bloom, arXiv:1910.03601.

[24] C. McIsaac, D. Keitel, T. Collett, I. Harry, S. Mozzon, O. Edy, and D. Bacon, Phys. Rev. D **102,** 084031 (2020).

[25] O. A. Hannuksela, K. Haris, K. K. Y. Ng, S. Kumar, A. K. Mehta, D. Keitel, T. G. F. Li, and P. Ajith, Astrophys. J. Lett. **874,** L2 (2019).

[26] X. Liu, I. Magana Hernandez, and J. Creighton, Astrophys. J. **908,** 97 (2021).

[27] L. Dai, B. Zackay, T. Venumadhav, J. Roulet, and M. Zaldarriaga, arXiv:2007.12709.

[28] R. Abbott *et al.* (LIGO Scientific and Virgo Collaborations), Astrophys. J. **923,** 14 (2021).

[29] J. M. Diego, T. Broadhurst, and G. Smoot, Phys. Rev. D **104,** 103529 (2021).

[30] T. Baker and M. Trodden, Phys. Rev. D **95,** 063512 (2017).

[31] S. Goyal, K. Haris, A. K. Mehta, and P. Ajith, Phys. Rev. D **103,** 024038 (2021).

[32] K.-H. Lai, O. A. Hannuksela, A. Herrera-Martín, J. M. Diego, T. Broadhurst, and T. G. F. Li, Phys. Rev. D **98,** 083005 (2018).

[33] J. M. Diego, Phys. Rev. D **101,** 123512 (2020).

[34] M. Oguri and R. Takahashi, Astrophys. J. **901,** 58 (2020).

[35] F. Xu, J. M. Ezquiaga, and D. E. Holz, Astrophys. J. **929,** 9 (2022).

[36] R. Abbott *et al.* (LIGO Scientific, Virgo, and KAGRA Collaborations), arXiv:2304.08393.

[37] M. Punturo *et al.*, Classical Quantum Gravity **27,** 084007 (2010).

[38] D. Reitze *et al.*, Bull. Am. Astron. Soc. **51,** 035 (2019), https://inspirehep.net/literature/1743201.

[39] P. Amaro-Seoane *et al.* (LISA Collaboration), arXiv:1702.00786.

[40] J. Luo *et al.* (TianQin Collaboration), Classical Quantum Gravity **33,** 035010 (2016).

[41] A. Klein *et al.*, Phys. Rev. D **93,** 024003 (2016).

[42] H.-T. Wang *et al.*, Phys. Rev. D **100,** 043003 (2019).

[43] Z. Gao, X. Chen, Y.-M. Hu, J.-D. Zhang, and S.-J. Huang, Mon. Not. R. Astron. Soc. **512,** 1 (2022).

[44] G. Cusin and N. Tamanini, Mon. Not. R. Astron. Soc. **504,** 3610 (2021).

[45] H. C. Ohanian, Int. J. Theor. Phys. **9,** 425 (1974).

[46] T. T. Nakamura, Phys. Rev. Lett. **80,** 1138 (1998).

[47] G. Boileau, N. Christensen, R. Meyer, and N. J. Cornish, Phys. Rev. D **103,** 103529 (2021).

[48] C. Leung, D. Jow, P. Saha, L. Dai, M. Oguri, and L. V. E. Koopmans, arXiv:2304.01202.

[49] J. M. Ezquiaga and M. Zumalacárregui, Phys. Rev. D **102,** 124048 (2020).

[50] C. Dalang, G. Cusin, and M. Lagos, Phys. Rev. D **105,** 024005 (2022).

[51] K. Yamamoto, Phys. Rev. D **71,** 101301 (2005).

[52] S. Hou, P. Li, H. Yu, M. Biesiada, X.-L. Fan, S. Kawamura, and Z.-H. Zhu, Phys. Rev. D **103,** 044005 (2021).

[53] A. J. Moylan, D. E. McClelland, S. M. Scott, A. C. Searle, and G. V. Bicknell, in *The Eleventh Marcel Grossmann Meeting on General Relativity* (World Scientific, Singapore, 2007), pp. 807–823.

[54] Z. Cao, L.-F. Li, and Y. Wang, Phys. Rev. D **90,** 062003 (2014).

[55] R. Takahashi, Astrophys. J. **835,** 103 (2017).

[56] P. Christian, S. Vitale, and A. Loeb, Phys. Rev. D **98,** 103022 (2018).

[57] L. Dai, S.-S. Li, B. Zackay, S. Mao, and Y. Lu, Phys. Rev. D **98,** 104029 (2018).

[58] S. Jung and C. S. Shin, Phys. Rev. Lett. **122,** 041103 (2019).

[59] K. Liao, M. Biesiada, and X.-L. Fan, Astrophys. J. **875,** 139 (2019).

[60] A. Mishra, A. K. Meena, A. More, S. Bose, and J. S. Bagla, Mon. Not. R. Astron. Soc. **508,** 4869 (2021).

[61] X.-C. Hu, X.-H. Li, Y. Wang, W.-F. Feng, M.-Y. Zhou, Y.-M. Hu, S.-C. Hu, J.-W. Mei, and C.-G. Shao, Classical Quantum Gravity **35,** 095008 (2018).

[62] S.-J. Huang, Y.-M. Hu, V. Korol, P.-C. Li, Z.-C. Liang, Y. Lu, H.-T. Wang, S. Yu, and J. Mei, Phys. Rev. D **102,** 063021 (2020).

[63] W. R. Brown, M. Kilic, A. Bédard, A. Kosakowski, and P. Bergeron, Astrophys. J. Lett. **892,** L35 (2020).

[64] W.-F. Feng, H.-T. Wang, X.-C. Hu, Y.-M. Hu, and Y. Wang, Phys. Rev. D **99,** 123002 (2019).

[65] M. L. Katz, L. Z. Kelley, F. Dosopoulou, S. Berry, L. Blecha, and S. L. Larson, Mon. Not. R. Astron. Soc. **491,** 2301 (2020).

[66] S. Liu, Y.-M. Hu, J.-d. Zhang, and J. Mei, Phys. Rev. D **101,** 103027 (2020).

[67] A. Klein *et al.*, arXiv:2204.03423.

[68] R. Buscicchio, A. Klein, E. Roebber, C. J. Moore, D. Gerosa, E. Finch, and A. Vecchio, Phys. Rev. D **104,** 044065 (2021).

[69] A. Toubiana, S. Marsat, S. Babak, J. Baker, and T. Dal Canton, Phys. Rev. D **102,** 124037 (2020).

[70] H.-M. Fan, Y.-M. Hu, E. Barausse, A. Sesana, J.-d. Zhang, X. Zhang, T.-G. Zi, and J. Mei, Phys. Rev. D **102,** 063016 (2020).

[71] X.-T. Zhang, C. Messenger, N. Korsakova, M. L. Chan, Y.-M. Hu, and J.-d. Zhang, Phys. Rev. D **105,** 123027 (2022).

[72] B. Wardell, A. Pound, N. Warburton, J. Miller, L. Durkan, and A. Le Tiec, Phys. Rev. Lett. **130,** 241402 (2023).

[73] Z.-C. Liang, Y.-M. Hu, Y. Jiang, J. Cheng, J.-d. Zhang, and J. Mei, Phys. Rev. D **105,** 022001 (2022).

[74] N. Bartolo *et al.* (LISA Cosmology Working Group), J. Cosmol. Astropart. Phys. 11 (2022) 009.

[75] C. Shi, J. Bao, H. Wang, J.-d. Zhang, Y. Hu, A. Sesana, E. Barausse, J. Mei, and J. Luo, Phys. Rev. D **100,** 044036 (2019).

[76] J. Bao, C. Shi, H. Wang, J.-d. Zhang, Y. Hu, J. Mei, and J. Luo, Phys. Rev. D **100,** 084024 (2019).

[77] L.-G. Zhu, Y.-M. Hu, H.-T. Wang, J.-d. Zhang, X.-D. Li, M. Hendry, and J. Mei, Phys. Rev. Res. **4,** 013247 (2022).

[78] C. Shi, M. Ji, J.-d. Zhang, and J. Mei, Phys. Rev. D **108,** 024030 (2023).

[79] M. Çalışkan, L. Ji, R. Cotesta, E. Berti, M. Kamionkowski, and S. Marsat, Phys. Rev. D **107,** 043029 (2023).

[80] G. Tambalo, M. Zumalacárregui, L. Dai, and M. H.-Y. Cheung, arXiv:2212.11960.

[81] D. Levin, Math. Comput. **38,** 531 (1982).

[82] A. I. Alfredo Deaño and Daan Huybrechs, *Computing Highly Oscillatory Integrals* (SIAM Publications, Philadelphia, PA, 2017), Chap. 2, https://epubs.siam.org/doi/abs/10.1137/1.9781611975123.

[83] X. Guo and Y. Lu, Phys. Rev. D **102,** 124076 (2020).

[84] G. Tambalo, M. Zumalacárregui, L. Dai, and M. H.-Y. Cheung, arXiv:2210.05658.

[85] R. Takahashi, Astron. Astrophys. **423,** 787 (2004).

[86] S. Khan, S. Husa, M. Hannam, F. Ohme, M. Pürrer, X. Jiménez Forteza, and A. Bohé, Phys. Rev. D **93,** 044007 (2016).

[87] The readers should not confuse the lensing amplification factor $F(f)$ with the detector antenna pattern functions $F_\alpha^+(t)$ and $F_\alpha^-(t)$.

[88] J. Ehlers and P. Schneider, in *Proceedings of the 13th Conference on General Relativity and Gravitation (GR-13)* (1993), pp. 21–40, https://inspirehep.net/literature/1624221.

[89] D. Sun and X. Fan, arXiv:1911.08268.

[90] L. Dai and T. Venumadhav, arXiv:1702.04724.

[91] P. Cremonese, J. M. Ezquiaga, and V. Salzano, Phys. Rev. D **104,** 023503 (2021).

[92] Y. Wang, R. K. L. Lo, A. K. Y. Li, and Y. Chen, Phys. Rev. D **103,** 104055 (2021).

[93] T. Morita and J. Soda, arXiv:1911.07435.

[94] P. Cremonese, D. F. Mota, and V. Salzano, Ann. Phys. (Berlin) **535,** 2300040 (2023).

[95] J. F. Navarro, C. S. Frenk, and S. D. M. White, Astrophys. J. **490,** 493 (1997).

[96] M. Bartelmann, Astron. Astrophys. **313,** 697 (1996), https://inspirehep.net/literature/415894.

[97] C. R. Keeton, arXiv:astro-ph/0102341.

[98] T. Robson, N. J. Cornish, and C. Liu, Classical Quantum Gravity **36,** 105011 (2019).

[99] C. Cutler and E. E. Flanagan, Phys. Rev. D **49,** 2658 (1994).